Materials LAB

RESEARCH ARTICLE

Materials Lab 2025, 4, 250104

Suppressing interfacial defects toward high-performance diffusion bonded FGH99 superalloy via a sandwich-structured interlayer

Xiaolong Hong, Zhiwei Qin*, Jiachen Li, Jilong Wang, Bingzhi Wang, Wenhao Wang, Fushuai Jin, Peng Li and Honggang Dong*

Interfacial voids and unbonded defects acted as stress concentration sites that significantly degraded the mechanical properties and directly compromised the structural integrity and service life of critical components. Herein, an innovatively Ni/$Cr_{0.625}$-$Al_{2.875}$/Ni sandwich-structured interlayer was designed to achieve high-quality diffusion bonding of FGH99 superalloy by regulating interfacial diffusion and recrystallization behavior. The results demonstrated that Ni foil effectively promoted the closure of interfacial voids and induced the formation of a graded interfacial structure, including the Ni transition zone (NTZ) and the interlayer diffusion zone (IDZ). This structure provided high-density grain boundaries as fast diffusion channels for elements, and served as an in-situ reaction container for the precipitation of γ′ strengthening phases. The shear strength of the joint with the sandwich-structured interlayer reached 857.7 MPa, which increased by 67.6 MPa compared to that of the single-layer interlayer. The fracture path of the joint transformed from the original bonding interface to the NTZ/IDZ interface. The fracture surface exhibited lots of fine dimples, indicating a transition from weak interfacial bonding to bulk strengthening and toughening of the joint. This work elucidated the mechanism of void closure and microstructural evolution mediated by the Ni interlayer, providing important theoretical support for the development of high-performance Ni-based superalloy diffusion bonding technology.

Ni-based superalloy had become key materials for hot end components of equipment such as aircraft engines and gas turbines due to their excellent high-temperature strength, creep resistance, and fatigue resistance[1–4]. With the continuous improvement of equipment performance, the overall manufacturing technology faced enormous challenges, employing diffusion bonding technology as a key method for manufacturing complex hollow turbine disks and repairing damaged components[5–7].

Due to the high-temperature stability, low diffusion coefficient, and surface oxide film barrier of Ni-based superalloy, it was easy to leave unbonded defects at the interface under conventional bonding parameters, including micro-voids and non-contact areas[8,9]. These defects, as sources of stress concentration, significantly reduced the fatigue life and high-temperature endurance strength of the joint, becoming potential failure factors for components in harsh service environments[10]. Therefore, using an interlayer was an effective way to achieve high-strength diffusion bonding. The contained activating elements can promote rapid atomic diffusion, thereby achieving a high-quality interface. Significantly, inappropriate interlayer selection not only failed to suppress these defects, but may also introduced new unbonded issues. The severe mismatch between the physical and chemical properties of the interlayer and the substrate can hinder effective atomic diffusion and interfacial voids closure, leading to more stubborn interfacial defects[11,12].

To eliminate these harmful defects, researchers were committed to finding optimized interlayers to precisely regulate the diffusion bonding process[13–18]. Although traditional brazing and TLP bonding techniques can achieve interface bonding, the brittle intermetallic compound phases (such as boride and silicide) constituted a weak interface, seriously damaging the high-temperature performance and reliability of the joint[19–21]. The use of pure metal foil interlayer with excellent plasticity and good compatibility to the substrate (such as Ti, Cu, Ni, etc.) had received widespread attention[22–27]. The core idea was to use the plastic deformation of the interlayer to preferentially fill the interface voids, and promote atomic interdiffusion through the interface composition gradient[28]. This strategy achieved interface metallurgical bonding and microstructure optimization. Ni foil was considered as an ideal candidate material for achieving high-quality bonding due to its perfect physical and chemical compatibility with Ni-based superalloy matrix and no risk of harmful phase formation. It was meaningful to further employ the behaviors of Ni foil for optimizing unbonded interface and develop strategies for avoiding the newly formed

School of Materials Science and Engineering, Dalian University of Technology, Dalian 116024, China

* Corresponding author, E-mail: qinzw@dlut.edu.cn ; donghg@dlut.edu.cn

Received 16 November 2025; Accepted 26 December 2025; Published online 29 January 2026

DOI: 10.54227/mlab.20250104

defects caused by insufficient atomic diffusion efficiency of traditional interlayers.

In this work, a novel Ni/$Cr_{0.625}$-$Al_{2.875}$/Ni sandwich-structured interlayer was designed to ameliorate the thermal mismatch of base metal (FGH99 superalloy) and the used interlayer through a Ni foil. Microstructural evolution and mechanical proprieties of the joints with Ni/$Cr_{0.625}$-$Al_{2.875}$/Ni sandwich-structured interlayer and $Cr_{0.625}$-$Al_{2.875}$ interlayer were investigated. The interfacial element diffusion behaviors and recrystallization mechanism induced by Ni foil were thoroughly elucidated, thereby establishing a transferable theoretical framework for the suitable bonding technology of advanced superalloys.

Materials and methods

Powder metallurgy Ni-based superalloy of FGH99 was used as the base metal for diffusion bonding and processed into small samples of 10 mm × 10 mm × 5 mm using wire cutting. The chemical composition of FGH99 superalloy was presented in Table 1. Cluster-plus-glue-atom model was used to design the composition of the interlayer. A series of interlayers with composition of $Ni_{11}Al_{3.5-x}CoCr_xNb_{0.25}Ta_{0.25}$ (x=0, 0.625, 1.25, 1.875) were designed by performing similar atomic substitution on [Al-Ni_{12}] Al_3 clusters using Cr, Co, Nb, and Ta elements, while the chemical composition of different interlayers was illustrated in Table 2. The raw materials (Ni, Al, Co, Cr, Nb and Ta, with a purity of 99.99%) were mixed according to the designed ratio and placed in a vacuum arc melting equipment (DHL-350) for repeated melting at least 8 times to ensure the preparation of a uniformly composed interlayer alloy ingot. The alloy ingot was prepared into an interlayer with a thickness of about 100 μm and dimensions of 12 mm × 12 mm through wire cutting, grinding, and polishing. According to the research of Guo et al.[29], a pure Ni foil with a thickness of 10 μm was used as a plastic transition layer to promote interface element diffusion and void closure.

Before the diffusion bonding, the FGH99 base metal was ground and polished to remove the oxide film on the surface of the sample to be bonded, and then cleaned with anhydrous ethanol ultrasonic for 15 min. The specimens, assembled in the configuration of FGH99/$Ni_{11}Al_{3.5-x}CoCr_xNb_{0.25}Ta_{0.25}$/FGH99 and FGH99/Ni/$Ni_{11}Al_{2.875}CoCr_{0.625}Nb_{0.25}Ta_{0.25}$/Ni/FGH99, were placed in a vacuum diffusion bonding furnace (ZTF2-10). A pressure of 20 MPa was subsequently applied under a vacuum of 6 × 10^{-3} Pa to ensure intimate contact between the samples. According to our previous research[30], heating was conducted at 10 °C min^{-1} to 800 °C with a 60 min holding time to achieve a uniform temperature, and then continued at the same rate to 1100 °C for a 120 min holding time, before furnace cooling to 80 °C.

The joints were wire-cut into 5 mm × 5 mm × 10 mm specimens for microstructural characterization and shear testing. Metallographic samples were ground and mechanically polished to a mirror finish. Microstructure and phases were characterized by field-emission SEM (ZEISS SUPRA 55, 15 kV) equipped with EBSD and TEM (JEOL JEM-2100F, 200 kV) with EDS, where the TEM samples were prepared by FIB (Helios G4 UX). Elemental homogenization and concentration of bonding area was analyzed by EDS. Compression shear tests were performed on three joints using a DNS-100 universal tester, and the resultant fracture morphologies were observed by SEM.

Results and discussion

Interfacial microstructure

Fig. 1 illustrated the interfacial microstructure using four different interlayers (Cr_0-$Al_{3.5}$, $Cr_{0.625}$-$Al_{2.875}$, $Cr_{1.25}$-$Al_{2.25}$, and $Cr_{1.875}$-$Al_{1.625}$) were bonded at 1100 °C/120 min/20 MPa. Continuous micro voids and unbound defects were observed at all four bonding interfaces, which can be attributed to the microplastic deformation and insufficient atomic diffusion at the bonding interfaces at 1100 °C (Fig. $1a_2$-$1d_2$). The unbonded zone at the bonding interface with Cr_0-$Al_{3.5}$ and $Cr_{0.625}$-$Al_{2.875}$ interlayer was relatively smaller. This indicated that the composition between Cr_0-$Al_{3.5}$ and $Cr_{0.625}$-$Al_{2.875}$ interlayer and FGH99 superalloy was relatively matched, which was conducive to the diffusion of interface elements (Fig. $1a_2$ and $1b_2$). The interface phase was analyze based on the EDS results in Table 3. The Ni/Cr_0-$Al_{3.5}$/Ni interlayer consisted of grayish-white block-like phase A and grayish-black dendritic phase B (Fig. $1a_1$). The chemical compositions of phases A and B were similar, with the Al and Ni element ratios being approximately 1:3. Therefore, phases A and B were confirmed as Ni_3Al phase. The phase A was rich in Ta element, and the phase B was rich in Nb element, because Ta and Nb atoms can occupy the B position of the A_3B-$L1_2$ structure[31,32]. The IZ with Ni/$Cr_{0.625}$-$Al_{2.875}$/Ni interlayer consisted of core-shell columnar phase (Fig. $1b_1$). The chemical compositions of phase C (shell) and D (core) were 18.89 at.% Al+67.59 at.% Ni+1.55 at.% Ta+1.61 at.% Nb and 19.22 at.% Al+68.61 at.% Ni+1.22 at.% Ta+1.07 at.% Nb, respectively. Therefore, phases C and D were also confirmed as Ni_3Al with Ta and Nb. The chemical

Table 1. Chemical composition of FGH99 superalloy (wt.%).

Alloy	Co	Cr	Mo	Ti	Al	Ta	W	Nb	C	Zr	B	Ni
FGH99	20.20	12.65	3.83	3.70	3.45	2.31	2.18	0.90	0.05	0.05	0.02	Bal.

Table 2. Chemical composition of different interlayers designed in this work.

Alloys	Mass fraction (wt. %)					
	Ni	Al	Cr	Co	Nb	Ta
$Ni_{11}Al_{3.5}CoNb_{0.25}Ta_{0.25}$	74.43	10.89	0	6.79	2.68	5.21
$Ni_{11}Al_{2.875}CoCr_{0.625}Nb_{0.25}Ta_{0.25}$	73.11	8.79	3.68	6.67	2.63	5.12
$Ni_{11}Al_{2.25}CoCr_{1.25}Nb_{0.25}Ta_{0.25}$	71.84	6.76	7.23	6.56	2.58	5.03
$Ni_{11}Al_{1.625}CoCr_{1.875}Nb_{0.25}Ta_{0.25}$	70.61	4.79	10.66	6.45	2.54	4.95

DOI: 10.54227/mlab.20250104

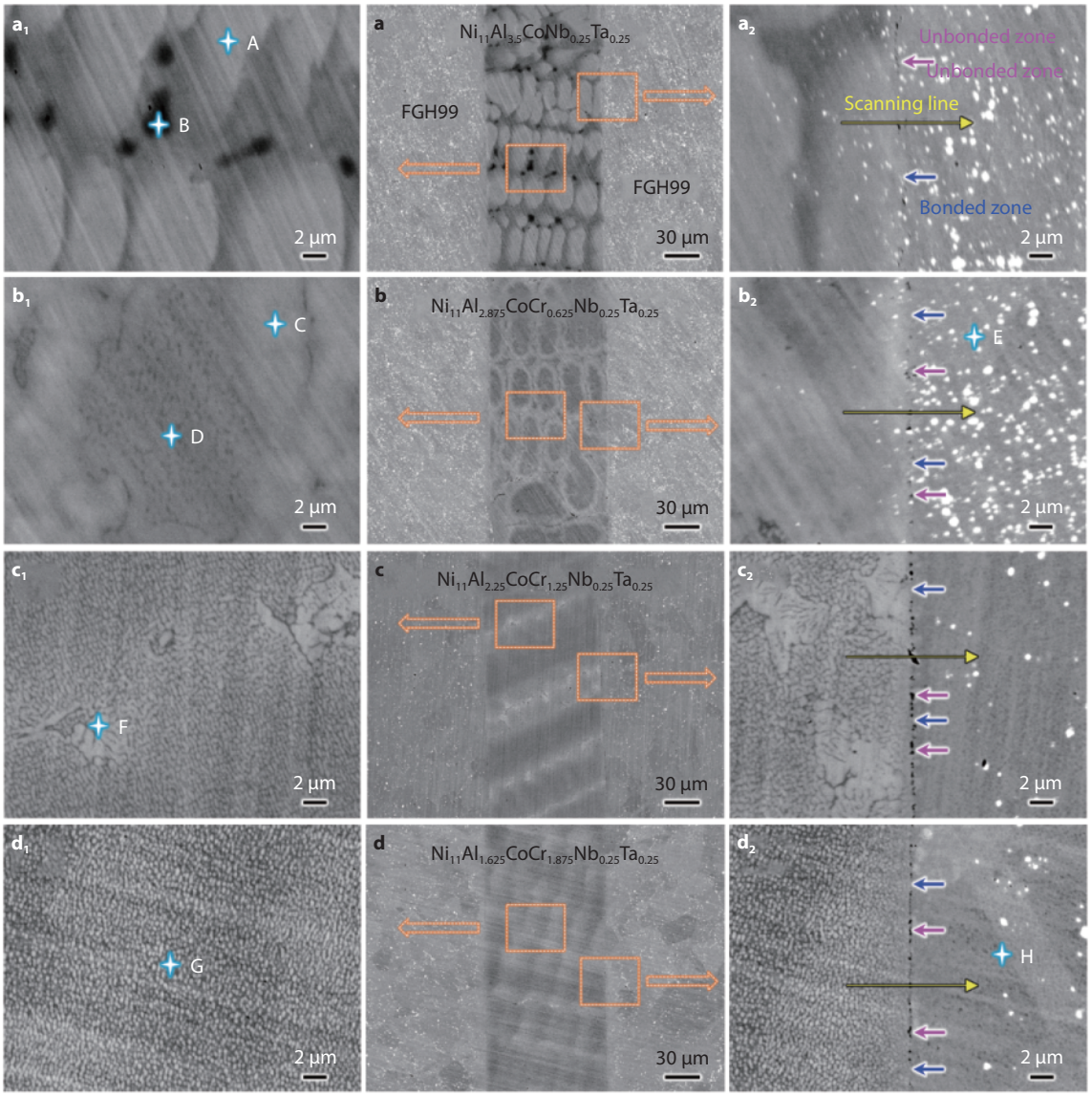

Fig. 1 Interface microstructure of FGH99 alloy was diffusion bonded by interlayers with different Cr content. **a-a$_2$** Cr_0-$Al_{3.5}$ interlayer. **b-b$_2$** $Cr_{0.625}$-$Al_{2.875}$ interlayer. **c-c$_2$** $Cr_{1.25}$-$Al_{2.25}$ interlayer. **d-d$_2$** $Cr_{1.875}$-$Al_{1.625}$ interlayer.

Table 3. Results of the point analysis of EDS (at.%) at the marked positions in Fig. 1.

Point	Al	W	Ta	Ni	Co	Cr	B	Zr	Nb	Mo	Ti	Possible phase
A	20.21	1.06	1.47	70.55	5.44	0.04	-	0.03	1.19	-	-	Ni_3(Al,Ta,Nb)
B	22.69	0.06	0.87	67.01	6.91	-	-	-	2.46	-	-	Ni_3(Al,Nb,Ta)
C	19.76	0.14	1.55	67.59	5.05	4.30	-	-	1.61	-	-	Ni_3(Al,Nb,Ta)
D	19.22	0.11	1.22	68.61	6.12	3.62	-	0.01	1.07	-	0.02	Ni_3(Al,Ta,Nb)
E	2.61	6.64	0.65	26.20	14.53	22.18	17.82	0.10	0.70	5.83	2.74	M_3B_2
F	14.29	0.05	1.56	64.14	7.82	9.81	-	-	2.33	-	-	Ni_3(Al,Nb,Ta)
G	10.68	0.04	1.15	66.06	9.26	11.76	-	-	1.05	-	-	Ni_3Al +$(Ni,Cr,Co)_{ss}$
H	7.26	0.76	0.69	49.27	19.18	15.23	-	0.02	0.55	2.62	4.42	Ni_3(Al,Ti)+$(Ni,Co,Cr)_{ss}$
I	18.81	0.14	1.15	68.29	6.33	3.27	-	-	2.01	-	-	Ni_3(Al,Nb,Ta)
J	17.57	0.08	1.52	69.41	6.27	3.94	-	0.01	1.17	-	0.03	Ni_3(Al,Ta,Nb)
K	8.36	0.04	0.56	78.31	6.74	4.56	-	-	0.58	0.03	0.83	Ni_3Al+Ni_{ss}
L	7.14	0.05	0.35	79.24	4.25	5.01	-	-	0.56	0.46	2.94	Ni_3(Al,Ti)+Ni_{ss}
M	3.92	0.64	0.79	47.82	15.38	11.02	-	0.35	1.83	1.77	16.48	$Ti_{3.3}Al$+$(Ni,Co,Cr)_{ss}$

DOI: 10.54227/mlab.20250104

composition of bright white particle phase E was 4.64 at.% W+22.18 at.% Cr+17.82 at.% B+5.93 at.% Mo (Fig. 1b$_2$). Phase E was confirmed as M_3B_2 boride with tetragonal crystal structure. According to the chemical composition of phase F existed in the IZ with $Cr_{1.25}$-$Al_{2.25}$ interlayer, the phase F was confirmed as Nb-rich Ni_3(Al, Nb, Ta) phase (Fig. 1c$_1$). With the further increase of Cr content (the decrease of Al content), the phase of the IZ with $Cr_{1.875}$-$Al_{1.625}$ interlayer was completely transformed into small particle γ'-Ni_3Al phase (point H) (Fig. 1d$_1$). The chemical composition of black blocky phase I was 7.26 at.% Al+49.27 at.% Ni+19.18 at.% Co +15.23 at.% Cr+4.42 at.% Ti (Fig. 1d$_2$). Phase I was confirmed as Ni_3(Al, Ti)+(Ni, Co, Cr)$_{ss}$ phases.

Fig. 2 presented the elemental line scan profiles across the joints fabricated with interlayers of varying Cr/Al compositions (Cr_0-$Al_{3.5}$, $Cr_{0.625}$-$Al_{2.875}$, $Cr_{1.25}$-$Al_{2.25}$, and $Cr_{1.875}$-$Al_{1.625}$). The interfacial regions exhibited distinct compositional partitioning, where the concentrations of Cr and Al varied systematically with the composition of the interlayer[33]. In all four interfaces, localized unbonded defects were identified by characteristic sharp compositional transitions: a concurrent depletion of Ni and Al alongside a pronounced enrichment of Cr. This elemental segregation implied the presence of oxide or impurity that hindered atomic diffusion and intimate contact during bonding. As indicated in Fig. 2a-b, d, an increase in Cr and O signals at certain interfacial voids suggested the formation of Cr-rich oxides. These oxides likely originated from surface adsorption or impurity introduced during processing. Meanwhile, the enrichment of W and C elements at voids in Fig. 2c indicated the precipitation of W-rich carbides, which was attributed to the segregation of slow-diffused W and C atoms at the interface during thermal cycle. The formation of these stable oxides and carbides at the interface exerted a strong pinning effect on the boundary migration between the FGH99 superalloy and the interlayer. This pinning effect stabilized the interfacial microstructure and significantly hindered the complete elimination of interfacial defects and the migration of grain boundaries during prolonged high-temperature exposure, thereby adversely affecting the interfacial integrity and mechanical performances.

To eliminate unbonded defects at the bonding interface, a Ni foil was introduced as a plastic interlayer. Based on prior experimental results, the interlayer with a composition of $Cr_{0.625}$-$Al_{2.875}$ exhibited the fewest defects and the highest joint strength. Therefore, a sandwich-structured interlayer with a Ni/$Cr_{0.625}$-$Al_{2.875}$/Ni configuration was designed and employed for diffusion bonding. Fig. 3a-c depicted the interfacial microstructure of the joint bonded at 1100 °C/120 min/20 MPa using this sandwich-structured interlayer. The interface appeared continuous and complete, with no evident voids or unbonded defects, indicating that the introduction of Ni foil effectively promoted atomic-level contact and diffusion across the interface. Thus, it achieved high-quality metallurgical bonding. According to the chemical composition analysis results in Table 3, phase I and phase C, as well as phase J and phase D, exhibited similar compositions. Thus, phase I was confirmed as Ni_3(Al, Nb, Ta) and phase J was confirmed as Ni_3(Al, Ta, Nb). Phase K contained 8.36 at.% Al and 0.83 at.%

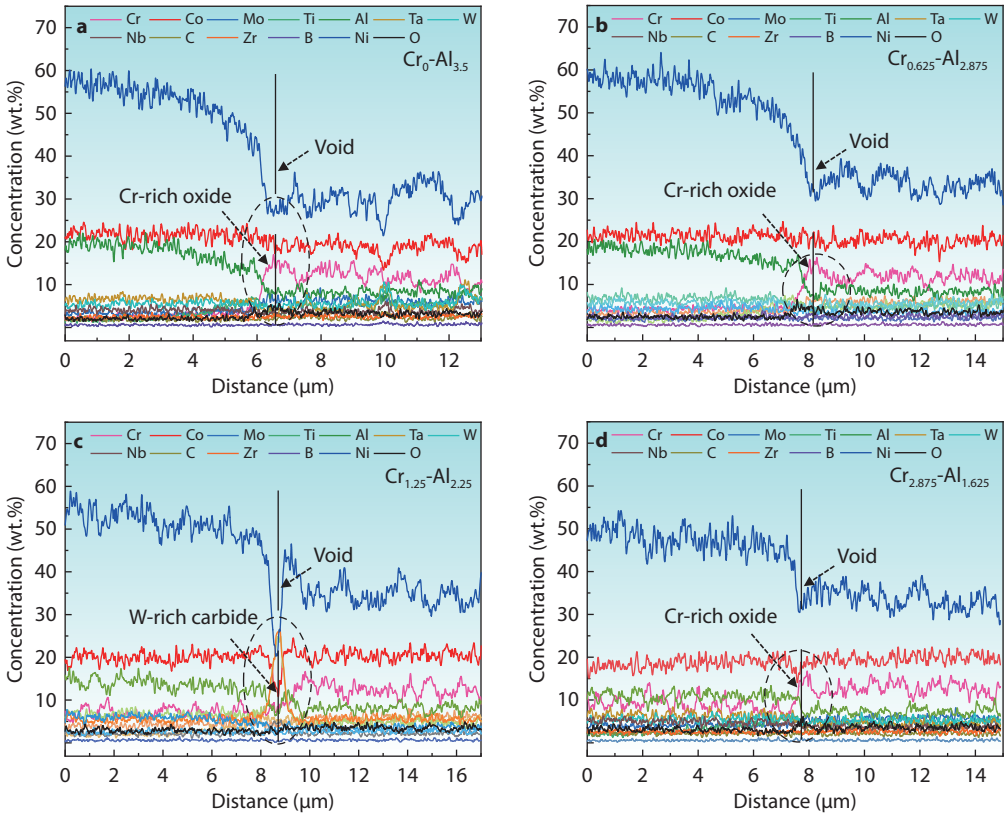

Fig. 2 Interfacial elemental line distribution of the joint bonded by interlayers with different Cr content. **a** Cr_0-$Al_{3.5}$ interlayer. **b** $Cr_{0.625}$-$Al_{2.875}$ interlayer. **c** $Cr_{1.25}$-$Al_{2.25}$ interlayer. **d** $Cr_{1.875}$-$Al_{1.625}$ interlayer.

DOI: 10.54227/mlab.20250104

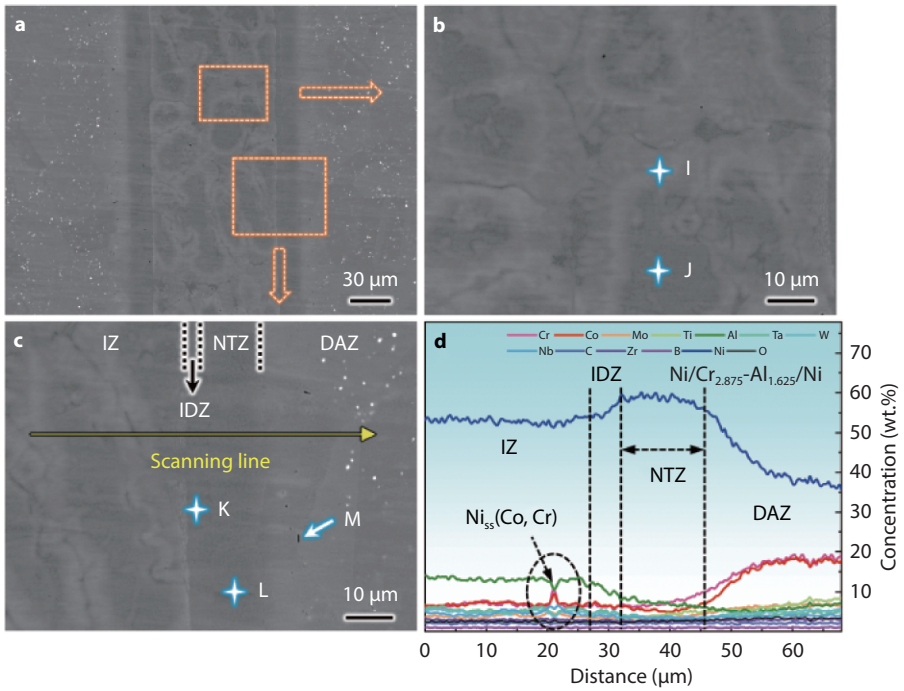

Fig. 3 Microstructure and elemental line distribution of the joint bonded with Ni/$Cr_{0.625}$-$Al_{2.875}$/Ni interlayer. **a** The cross-section image of typical interface. **b** The magnified view of zone in (a). **d** The elemental line distribution in (c).

Ti, while phase L contained 7.14 at.% Al and 2.94 at.% Ti. Phase K was located near the interlayer, and phase L was close to the diffusion zone. It can be concluded that phase K consisted of Ni_3Al + γ-Ni solid solution (Ni_{ss}), and phase L consisted of $Ni_3(Al, Ti)$ + Ni_{ss}. Additionally, phase M was rich in Ni (47.82 at.%), Ti (16.48 at.%), Co (15.38 at.%), and Cr (11.02 at.%), with an Al content of 3.92 at.%. The atomic ratio of Ti to Al was approximately 3.3:1, which revealed that this region was a $Ti_{3.3}Al$ + $(Ni, Co, Cr)_{ss}$ phases. Based on the microstructural and compositional analysis, the diffusion-bonded interface can be divided into the interlayer zone (IZ), the Ni transition zone (NTZ), the interlayer diffusion zone (IDZ), and the diffusion-affected zone (DAZ). The interfacial zoning characteristics can also be identified from the elemental line distribution map (Fig. 3d). The corresponding elemental line distribution further exhibited a smooth compositional transition across the interface. Notably, the localized enrichments of Co and Cr within the ellipsoid-marked regions suggested the formation of Ni_{ss}(Co, Cr) phase. The IDZ primarily resulted from interdiffusion between the interlayer and the Ni foil, leading to the formation of numerous fine γ′-Ni_3Al precipitates[34]. The NTZ was formed mainly by the diffusion of Al and Ti (γ′-forming elements) from the FGH99 base metal into the Ni foil, resulting in the precipitation of fine γ′-$Ni_3(Al, Ti)$ precipitates. Therefore, the Ni foil not only acted as a plastic buffer layer to mitigate interfacial strain caused by thermal mismatch, but also helped establish a gradual compositional gradient, facilitating directly elemental diffusion and redistribution near the interface[35]. More importantly, the Ni foil served as an in-situ reaction container, providing favorable conditions for the uniform and fine precipitation of γ′ strengthening phases. This significantly enhanced the microstructural homogeneity and mechanical properties of the interfacial region.

Fig. 4 illustrated a detailed examination of the interfacial microstructure in the DAZ with Ni/$Cr_{0.625}$-$Al_{2.875}$/Ni interlayer bonded at 1100 °C for 120 min. The compact bonding interface without nano-voids was obtained, and two types of nano-precipitates were formed at the bonding interface (Fig. 4a). The phases on the DAZ of the joint in Fig. 4a were identified as $Ti_{3.3}Al_{[0\bar{1}\bar{3}]}$, $L1_2$-$\gamma'_{[\bar{1}\bar{1}0]}$ and FCC-$\gamma_{[\bar{1}\bar{1}0]}$ phases by SAED, respectively (Fig. 4b-d). The SAED images also proved that $L1_2$-$\gamma'_{[\bar{1}\bar{1}0]}$ nano-phase and FCC-$\gamma_{[\bar{1}\bar{1}0]}$ matrix was coherent. The contribution of $L1_2$-γ′ nanoparticles coherent with the matrix can be described by the shear mechanism. The antiphase boundary (APB) was formed when the dislocation sheared the ordered precipitated phase[36]. The proportion of $L1_2$ precipitated phase in the interface was larger, thus, the shear mechanism played a dominant role in improving the strength of the joint. The HRTEM image of the interface between $Ti_{3.3}Al$ and FCC-γ was observed in Fig. 4e. The IFFT image (Fig. 4g) was obtained based on the $[00\bar{2}]$ crystal plane of FCC-γ and $[\bar{3}3\bar{1}]$ crystal plane of $Ti_{3.3}Al$ of the FFT image (Fig. 4f) in the pink area of Fig. 4e. The corresponding crystal plane spacings of FCC-$\gamma_{[00\bar{2}]}$ and $Ti_{3.3}Al_{(\bar{3}3\bar{1})}$ were calibrated to 0.2137 nm and 0.2568 nm, respectively, through the intensity line profiles of individual atomic columns (Fig. 4i-j). According to the calculation formula for lattice mismatch[37,38], the lattice mismatch of the two-phase interface was calculated to be 18.32%, indicating an incoherent interface. Fig. 4h demonstrated the corresponding lattice stripe reconstruction image. Significant distortion was observed on the $(\bar{3}3\bar{1})$ crystal plane on the $Ti_{3.3}Al$ side, which indicated copious strain energy was stored in the $Ti_{3.3}Al$ phase.

The interface behaviors and recrystallization were closely related during the diffusion bonding of Ni/$Cr_{0.625}$-$Al_{2.875}$/Ni in-

DOI: 10.54227/mlab.20250104

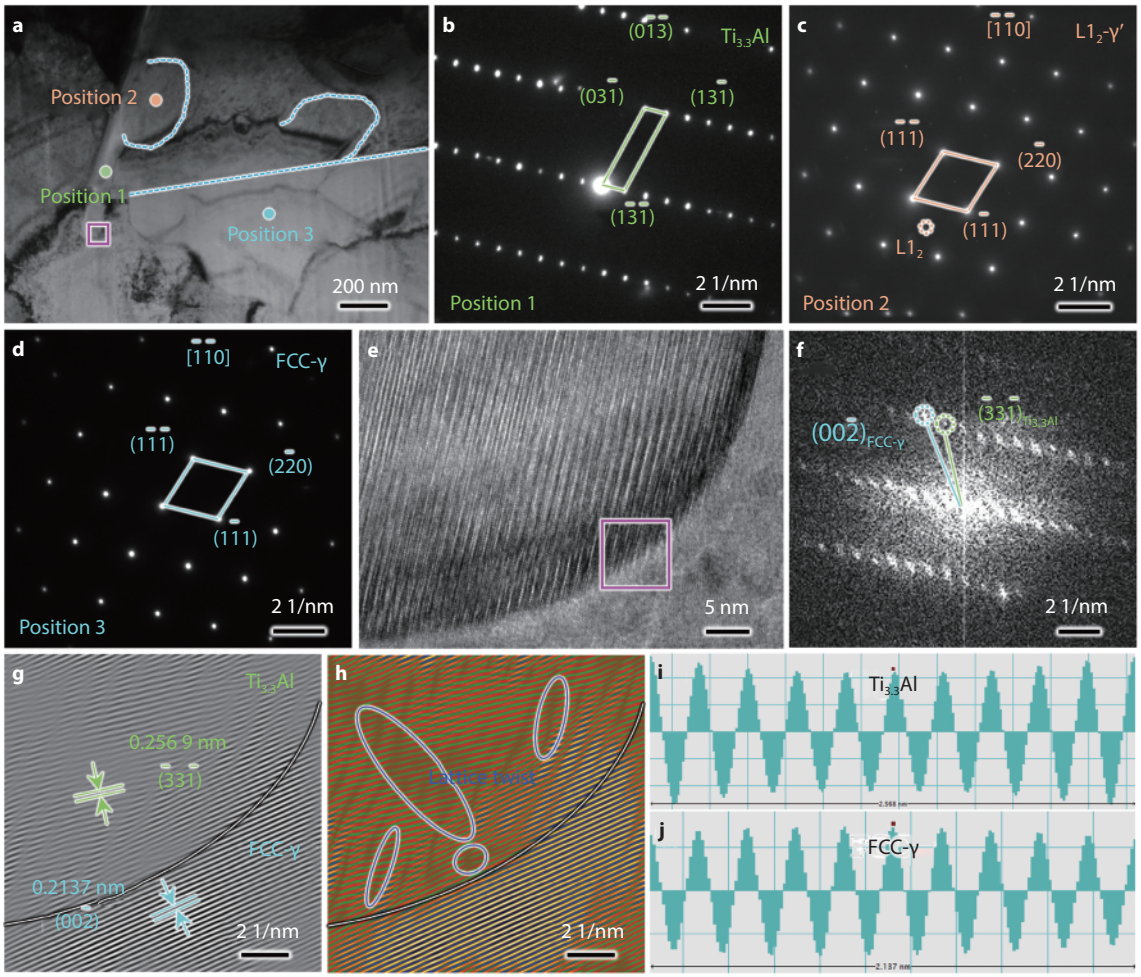

Fig. 4 Atomic scale characterization of the interface in the DAZ of the joint bonded with Ni/$Cr_{0.625}$-$Al_{2.875}$/Ni interlayer under thermo-mechanical coupling. **a** Bright-field TEM image. **b-d** SAED patterns corresponding to the marked locations in **a**. **e** HRTEM image of pink region in **a**. **f** FFT and **g** IFFT pattern of pink region in **e**. **h** The corresponding lattice fringe reconstruction image of **g**. Intensity line profiles of individual atomic columns of **i** $Ti_{3.3}Al$ and **j** FCC-γ.

terlayer. Fig. 5 depicted the EBSD results of the joint bonded with the Ni/$Cr_{0.625}$-$Al_{2.875}$/Ni interlayer. Fig. 5a showed that the interface was composed of a series of newly formed grain boundaries interconnected, with an average grain size of 11.13 μm (Fig. 5f). The initial interface gaps between the interlayer, Ni foil, and FGH99 superalloy were eliminated through the interdiffusion of elements such as Cr, Al, Ni, and Ti. Fig. 5d illustrated that the area proportions of recrystallized grain and substructure at the interface were 53.2% and 46.7%, respectively. During the diffusion bonding, the concentration gradient and thermal stress generated by diffusion in the interface and near interface regions provided the driving force for recrystallization[39,40]. The original deformed grain (or substructure induced by bonding pressure) gradually formed new recrystallized grain without strain through mechanisms such as grain boundary migration and dislocation rearrangement[41–43]. During the recrystallization, the newly formed grain not only refined the interface structure, but also replaced the physical separation of the initial interface through the extensive formation of high angle grain boundaries (HAGBs) (accounting for 94.9%) (Fig. 5c, h). The excellent migration ability of HAGBs further promoted the uniform diffusion of elements and effectively suppresses the segregation of interface component. The pole figure (PF) plot demonstrated a pole density of 19.07, which reflected significant preferential orientation characteristics of grains in the interface region (Fig. 5e). The lower misorientation (KAM_{ave}=0.27°) inside the recrystallized grains (Fig. 5b, g) reduced the internal stress in the interface region, avoiding interface cracking caused by stress concentration. The final interface transformed from initial physical contact to a stable metallurgical bond, giving the diffusion bonding interface good bonding strength and structural stability.

Fracture analysis

The shear strength of FGH99 superalloy joints diffusion-bonded using different interlayers were summarized in Fig. 6. The direct diffusion-bonded FGH99 joint achieved a shear strength of 720.8 MPa, while the joint with a Cr-free interlayer exhibited lower strength. With the introduction of Cr into the interlayer, the joint shear strength exceeded that of the direct-bonded joint, despite the presence of micro-voids and localized unbonded defects at the interface. This improvement was attributed to the role of Cr in regulating the activity

DOI: 10.54227/mlab.20250104

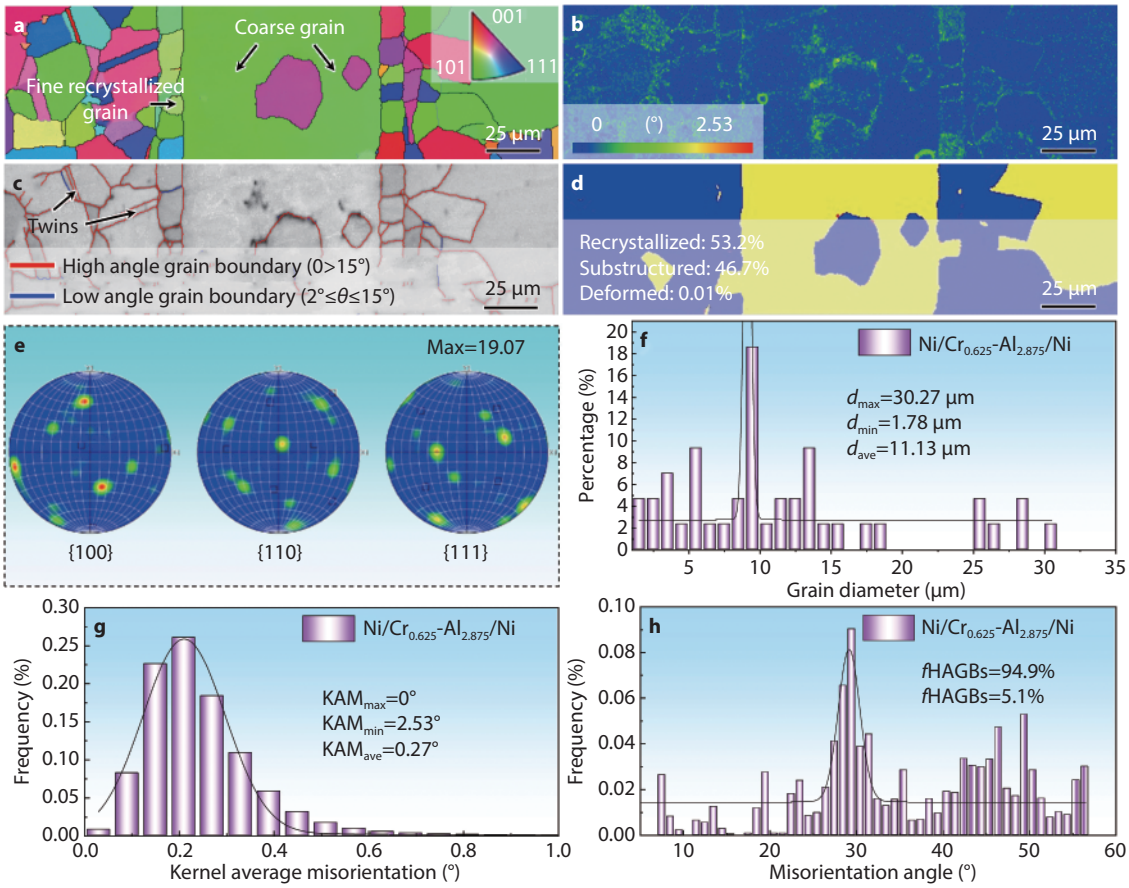

Fig. 5 EBSD analysis results of the interface diffusion bonded with Ni/$Cr_{0.625}$-$Al_{2.875}$/Ni interlayer. **a** The results of inverse pole figure (IPF) and **f** The distribution of grain size. **b** The distribution of Kernel Average Misorientation (KAM) mapping and **g** its corresponding statistical results. **c** The distribution of HAGBs and low angle grain boundaries (LAGBs) and **h** its corresponding statistical results. **d** The distribution of recrystallized grain, substructure and deformed grain. **e** The results of PF.

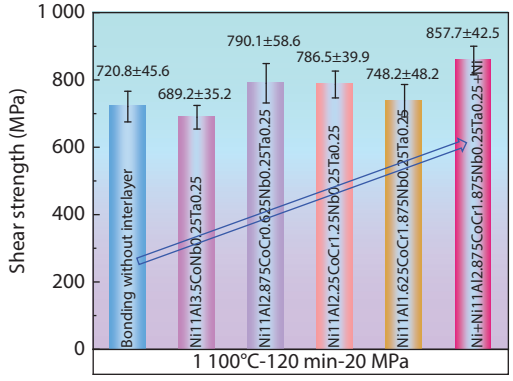

Fig. 6 The shear strength of the joints with different interlayers bonded at 1100 °C-120 min-20 MPa.

and diffusion paths of elements such as Al and Ti. Moreover, the high affinity of Cr for oxygen helped mitigate the detrimental effects of surface oxide films during bonding, thereby enhancing interfacial integrity. Notably, the joint with the Ni/$Cr_{0.625}$-$Al_{2.875}$/Ni sandwich-structured interlayer exhibited a significant increase in shear strength, reaching 857.7 MPa. This result clearly demonstrated the effectiveness and superiority of the functionally graded sandwich-structured interlayer designed in this work. Future work will focus on the high-temperature bonding behavior of this sandwich-structured interlayer to facilitate its implementation in diffusion bonding of advanced superalloys.

Fig. 7a-d demonstrated the fracture path of FGH99 superalloy joint without using Ni foil as a transition layer. The fracture paths all occurred in the bonding interface area, and the main reason can be attributed to the presence of voids and unbound defects at the interface. After adopting the Ni/$Cr_{0.625}$-$Al_{2.875}$/Ni sandwich-structured interlayer, the fracture path of the joint underwent a significant change, expanding along the interface between NTZ and IDZ. The fracture morphology showed a more tortuous feature, as depicted in Fig. 7e.

Fig. 8 illustrated the fracture morphology of the joints obtained using single-layer $Cr_{0.625}$-$Al_{2.875}$ and Ni/$Cr_{0.625}$-$Al_{2.875}$/Ni sandwich-structured interlayer, respectively. For the joint using only the $Cr_{0.625}$-$Al_{2.875}$ interlayer, the fracture surface exhibited a mixed feature of tearing edges and a small number of toughness dimples, which was due to the plastic deformation and separation of the local bonding area at the interface under shear stress. Based on the chemical composition analysis results in Table 4, the A, B, and C phases presented on the fracture surface were identified as the γ' + $(Ni, Co, Cr)_{ss}$ phases, confirming that the fracture occurred at the interface between the interlayer and the base metal. The joint with

DOI: 10.54227/mlab.20250104

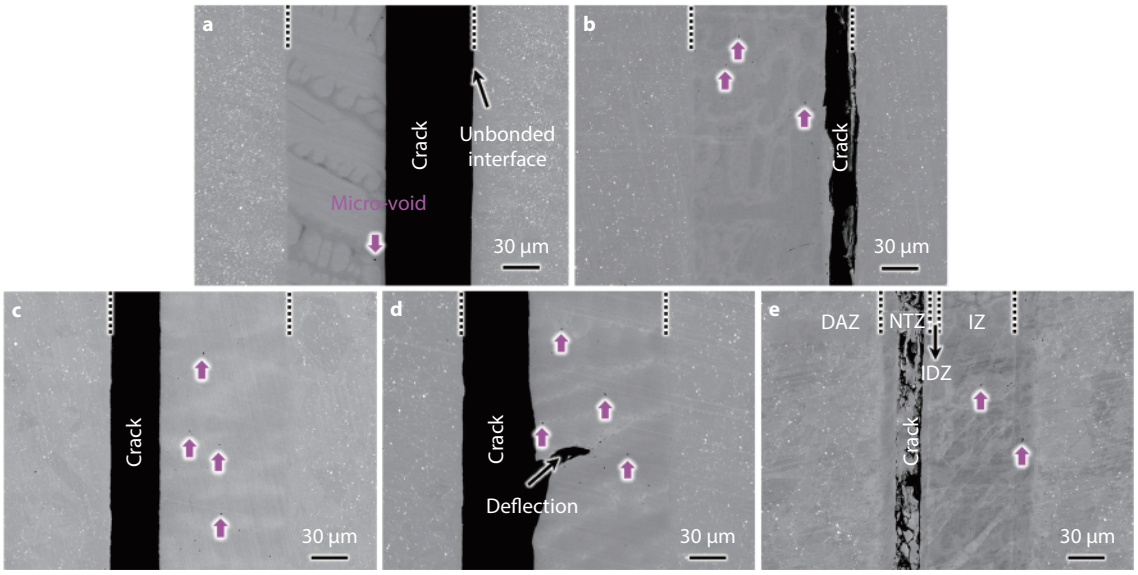

Fig. 7 Fracture paths of the joints with different interlayers. **a** Cr_0-$Al_{3.5}$ interlayer. **b** $Cr_{0.625}$-$Al_{2.875}$ interlayer. **c** $Cr_{1.25}$-$Al_{2.25}$ interlayer. **d** $Cr_{1.875}$-$Al_{1.625}$ interlayer. **e** Ni/$Cr_{0.625}$-$Al_{2.875}$/Ni interlayer.

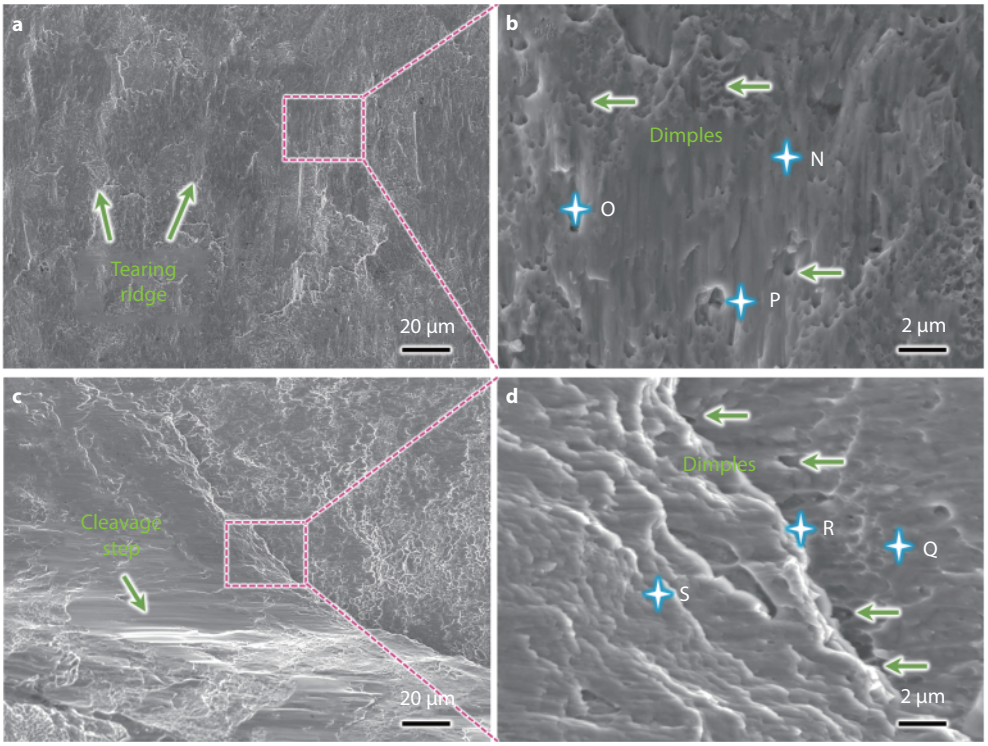

Fig. 8 Fracture morphology of the joints with **a-b** $Cr_{0.625}$-$Al_{2.875}$ and **c-d** Ni/$Cr_{0.625}$-$Al_{2.875}$/Ni interlayer.

Ni/$Cr_{0.625}$-$Al_{2.875}$/Ni sandwich-structured interlayer exhibited a fracture morphology characterized by the coexistence of cleavage steps and numerous small dimples. These high-density small dimples increased the effective fracture area, which indicated that crack propagation requires more energy consumption, resulting in a significant improvement in joint strength macroscopically[44–46]. The components of D, E, and F phases on the fracture surface were identified as Ni_{ss} phase and $\gamma' + Ni_{ss}$ phases, respectively, indicating that the fracture location had shifted to the vicinity of NTZ. The migration of this fracture path and the increase in the number of toughness dimples were attributed to the effective regulation of interface reactions by the introduction of Ni foil, which promoted the plastic deformation ability of the joint.

Interface void closure mechanism

Interfacial voids constituted a critical factor limiting the joint strength during diffusion bonding, underscoring the importance of investigating voids closure mechanisms[47]. In this work, the introduction of a Ni foil as transition layer signific-

DOI: 10.54227/mlab.20250104

Table 4. Results of the EDS point analysis (at.%) for the marked positions in Fig. 8.

Point	Al	Ti	Cr	Co	Ni	Zr	Nb	Mo	Ta	W	Possible phase
N	9.75	3.44	14.38	17.92	49.59	0.00	0.63	2.39	0.93	0.97	γ'+(Ni,Co,Cr)$_{ss}$
O	12.19	3.91	13.26	17.07	47.20	1.75	0.67	2.01	1.10	0.84	γ'+(Ni,Co,Cr)$_{ss}$
P	10.42	3.82	13.59	17.73	48.93	0.26	0.65	2.32	1.07	1.21	γ'+(Ni,Co,Cr)$_{ss}$
Q	0.88	0.36	2.02	3.98	92.64	0.04	0.02	0.00	0.04	0.02	Ni$_{ss}$
R	1.75	0.13	1.21	3.69	93.11	0.00	0.02	0.00	0.07	0.02	Ni$_{ss}$
S	3.20	0.68	2.18	3.30	90.13	0.00	0.20	0.00	0.25	0.06	γ'+Ni$_{ss}$

antly enhanced the closure of interfacial voids. Based on the observed morphological evolution of interfacial voids during bonding, a mechanism for void closure was proposed, as illustrated in Fig. 9. During the initial stage of diffusion bonding, localized plastic deformation occurred upon contact between the two surfaces. Owing to surface roughness, the actual contact area was limited (Fig. 9a), resulting in stress concentration at asperities. The curvature difference between the contact asperities and the void surfaces induced a chemical potential gradient, which acted as the driving force for surface diffusion of atoms toward the interface[48]. As depicted in Fig. 9b, activated atoms migrated directionally from regions of higher chemical potential to those of lower chemical potential, thereby progressively filling the interfacial voids. The volume transfer rate ($\dot{V}$) was given as[49]:

$$\dot{V} = \frac{2A_s D\Omega\gamma}{r_1 kT}\left(\frac{1}{r_1} - \frac{1}{R_1}\right) \quad (1)$$

Where D is the diffusion coefficient, A_s is the surface diffusion area, Ω is the atomic volume, k is the average surface curvature, γ is the surface tension, and T is the absolute temperature. r_1 *and* R_1 are the short and long axes of the gap, respectively. When pressure was applied, a stress gradient ($\partial\sigma/\partial x$) appeared along the bonding interface near the voids. Atomic diffusion occurred in the stress gradient region, as shown in Fig. 9b. The stress induced atoms flux (J_{stress}) along the interface can be described by the following formula[50]:

$$J_{stress} = \frac{-D}{\Omega kT}\left(\Omega\frac{\partial\sigma}{\partial x}\right) \quad (2)$$

As the bonding temperature increased, a significant temperature gradient was formed in the initial contact area. The

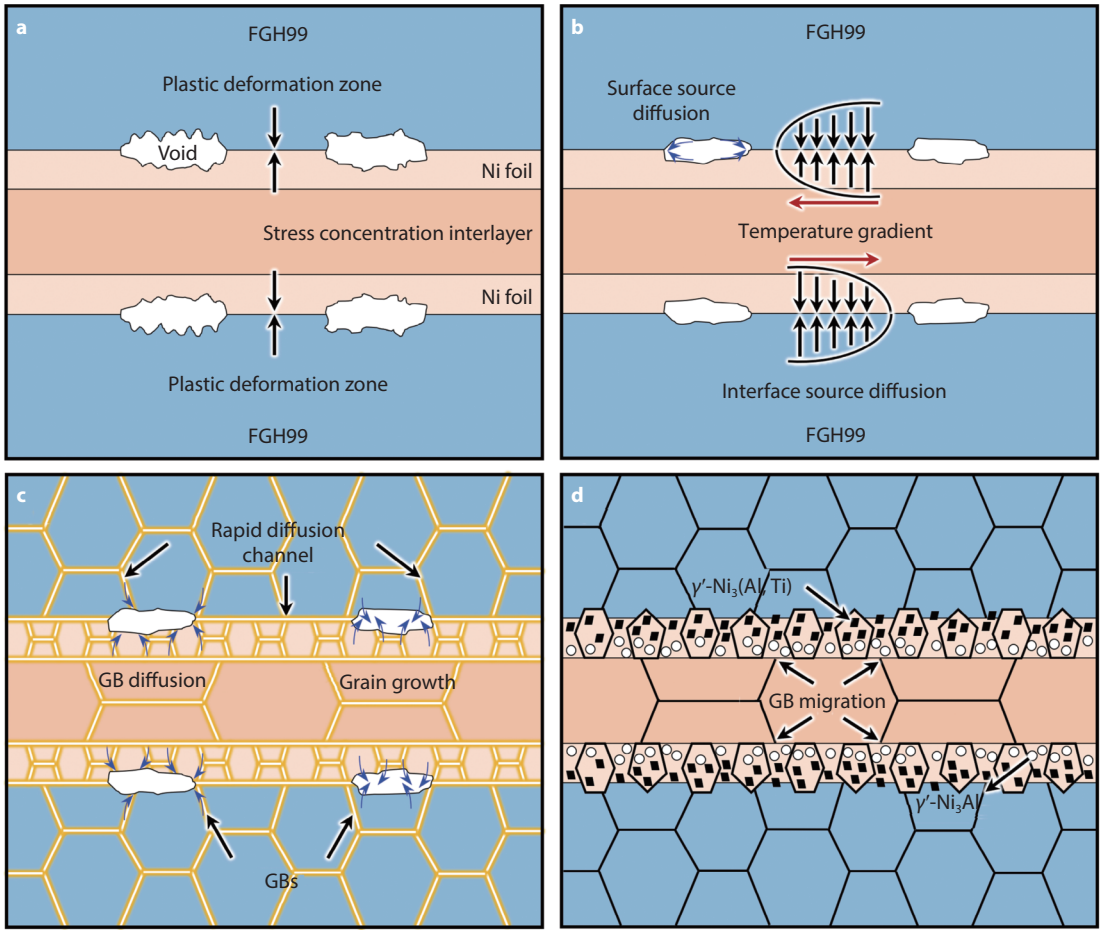

Fig. 9 Schematic diagram of the joint with sandwich-structured interlayer. **a** Initial plastic deformation. **b** Surface source diffusion and interface source diffusion. **c** GB diffusion and grain growth. **d** Well bonded joint with alternating coarse- and fine-grain layers, γ'-Ni_3Al phase, and γ'-Ni_3(Al,Ti) phase.

DOI: 10.54227/mlab.20250104

heat induced atomic flux ($J_{thermal}$) can be expressed as

$$J_{\text{thermal}} = \frac{-D}{\Omega kT}\left(\frac{Q^*}{T}\frac{\partial T}{\partial x}\right) \quad (3)$$

Here, $\partial T/\partial x$ is the temperature gradient at the bonding interface near the gap, and Q^* is the atomic transfer heat. Combining Eqs. (2) and (3), the total interface source diffusion flux (J) can be described as follows:

$$J = \frac{-fC_v \exp\left(-\frac{Q - C|Z^*|e\tau I}{RT}\right)}{\Omega kT}\left(\Omega\frac{\partial \sigma}{\partial x} + \frac{Q^*}{T}\frac{\partial T}{\partial x}\right) \quad (4)$$

The thermomechanical coupling effect during diffusion bonding promoted dislocation recovery and grain rotation at the interface, leading to the formation of contact surfaces. Following the establishment of these contact areas, the combined action of the thermal gradient across the interface and the compositional gradient established by the Ni foil enhanced the atomic flux, thereby inducing accelerated interdiffusion of elements from both sides. This process effectively intensified both surface diffusion and interfacial diffusion, which consequently facilitated the closure of microscopic interfacial voids.

The growth of grains along the interior of the voids in Ni foil also promoted the closure of voids during the bonding process (Fig. 9c), and the void closure rate $\left(\frac{dR}{dt}\right)$ can be expressed as[51]:

$$\frac{dR}{dt} = -MP\exp\left(-\frac{\Delta G_{void}}{k_b T}\right) \quad (5)$$

In the equation, M is the migration rate of grain boundaries, P is the driving force for GB migration, ΔG_{void} is the energy barrier for void closure, and k_b is the Boltzmann constant. M and P can be estimated as the following equation:

$$M \approx \frac{D\Omega}{2\delta k_b T} = \frac{fC_v\Omega}{2\delta k_b T}\exp\left(-\frac{Q - C|Z^*|e\tau I}{RT}\right) \quad (6)$$

$$P = \frac{2\gamma_{gb}}{d} \quad (7)$$

Where d is the average grain size and γ_{gb} is GB energy. According to Eqs. (5) - (7), the void closure rate can be expressed as follows:

$$\frac{dR}{dt} = -\frac{fC_v\Omega}{2\delta k_b T}\exp\left(-\frac{Q - C|Z^*|e\tau I}{RT}\right)\frac{2\gamma_{gb}}{d}\exp\left(-\frac{\Delta G_{void}}{k_b T}\right) \quad (8)$$

According to Eq. (8), the fine grains (smaller d-value) within the NTZ facilitated void closure. Grain boundaries (GBs) can serve as fast diffusion channels for elements. The driving force for GB diffusion included concentration gradients, temperature gradients, and stress gradients along the GBs near the voids. As shown in Fig. 5c, the bonding interface contained a high proportion of HAGBs, which significantly enhanced the diffusion rate of elements such as Al and Ti from the interlayer and base metal along the GBs. This accelerated diffusion promoted the in-situ precipitation of a large number of γ' strengthening phases within the NTZ, as illustrated in Fig. 9d.

Conclusions

This work successfully achieved high-strength diffusion bonding of FGH99 superalloy by introducing a sandwich-structured Ni/$Cr_{0.625}$-$Al_{2.875}$/Ni interlayer. The results demonstrated that the sandwich-structured interlayer played a critical role in interfacial voids closure and microstructural optimization. Under thermo-mechanical coupling, the Ni foil preferentially filled macroscopic voids through plastic deformation, while curvature-driven surface diffusion and stress gradient-dominated interfacial diffusion collectively contributed to the rapid filling of microscopic voids. The interfacial recrystallization process generated a high proportion of HAGBs, which provided fast diffusion channels for γ′-forming elements such as Al and Ti, promoting the in-situ precipitation of numerous fine γ′ strengthening phases and significantly enhancing the interfacial region. Compared with the single-layer interlayer, the sandwich-structured interlayer effectively eliminated continuous micro-voids and unbonded regions at the interface, achieving dense metallurgical bonding and a joint shear strength of 857.7 MPa. The fracture path shifted from the original bonding interface to the NTZ/IDZ interface, with the fracture surface exhibiting high-density fine dimples. This study systematically elucidated the optimization mechanism of the sandwich-structured interlayer, providing important theoretical and experimental foundation for the development of diffusion bonding technology for superalloy.

■ AUTHOR CONTRIBUTIONS

Xiaolong Hong: Conceptualization, Methodology, Investigation, Formal analysis, Validation, Writing - original draft, Writing - review & editing. **Zhiwei Qin:** Formal analysis, Conceptualization, Data curation, Validation, Writing - review & editing. **Jiachen Li:** Formal analysis, Methodology, Data curation, Investigation, Supervision. **Jilong Wang:** Conceptualization, Formal analysis, Software, Investigation. **Bingzhi Wang:** Resources, Methodology, Data curation. **Wenhao Wang:** Methodology, Resources, Investigation. **Fushuai Jin:** Investigation. **Peng Li:** Methodology, Supervision, Validation, Investigation. **Honggang Dong:** Funding acquisition, Conceptualization, Methodology, Resources, Project administration, Writing - review & editing.

■ ACKNOWLEDGMENTS

This work was financially supported by National Natural Science Foundation of China (Nos. 52575361, 52275314, and 52504402).

■ CONFLICTS OF INTEREST

There are no conflicts of interest to declare.

■ REFERENCES

1. D. Zhang, W. Liu, Y. Li, D. Sun, Y. Wu, S. Luo, S. Chen, Y. Tao, B. Zhang, *Nat. Commun.*, 2023, 14, 2961.
2. C. C. Silva, R. S. Silva, É. M. Miná, M. F. Motta, H. C. Miranda, G. Dalpiaz, R. R. Marinho, M. T. P. Paes, A. K. da Silva, I. Wossack, C. H. Liebscher, *J. Mater. Sci. Technol.*, 2026, 254, 168–179.
3. H. Xu, Z. J. Zhang, P. Zhang, C. Y. Cui, T. Jin, Z. F. Zhang, *Sci. Rep.*, 2017, 7, 8046.
4. M. Sakaguchi, K. Mase, I. Sasakura, S. Tanaami, T. Fukuda, *Int. J. Fatigue.*, 2026, 203, 109309.

DOI: 10.54227/mlab.20250104

5. O. Takakuwa, Y. Ogawa, R. Miyata, *Sci. Rep.*, 2023, 13, 6804.
6. Y. Chen, Z. Yao, H. Wang, J. Dong, J. Peng, M. Ren, H. Yang, L. Leng, *Eng. Fail. Anal.*, 2025, 179, 109797.
7. T. Wu, C. Wang, Y. Liu, Q. Zhang, P. Lin, X. Yue, T. Lin, P. He, *J. Mater. Sci. Technol.*, 2025, 226, 181–195.
8. Y. Ding, D. Wen, X. Wang, B. Kong, Z. Gong, Y. Wang, H. Lai, Y. Xu, X. Yang, S. Wang, Y. Sun, *Int. J. Refract. Met. Hard Mater.*, 2025, 133, 107302.
9. R. Chang, Q. Guo, Z. Ma, R. Ding, C. Liu, Y. Liu, *Acta Mater.*, 2024, 276, 120121.
10. C. Li, Y. Li, D. Zhang, X. Li, W. Zhao, *J. Mater. Res. Technol.*, 2023, 26, 4042–4058.
11. T. Wu, Y. Liu, Q. Zhang, K. Li, R. Xu, H. He, C. Wang, P. Lin, X. Yue, T. Lin, P. He, *J. Manuf. Process.*, 2024, 128, 60–71.
12. J. Lin, X. Li, C. Wang, R. Xu, X. Zhang, F. Lu, P. Lin, H. Mei, Y. Liu, Y. Zhuang, P. He, T. Lin, *Compos. Part. B. Eng.*, 2023, 260, 110771.
13. J. Wang, Z. Qin, P. Li, Z. Ding, P. Zhao, B. Wang, X. Ma, H. Sun, Y. Cheng, Y. Chang, H. Dong, *Intermetallics*, 2025, 185, 108916.
14. S. Zhao, B. Shao, H. Chen, Y. Hu, Z. Pan, Y. Liu, P. Wang, X. Song, W. Li, *J. Mater. Sci. Technol.*, 2025, 233, 223–238.
15. P. Wang, W. Liu, L. Gu, H. Ran, X. Song, Z. Pan, H. Chen, W. Li, *Trans. Mater. Res.*, 2025, 1, 100012.
16. P. Wang, W. Shi, L. Gu, H. Ran, Z. Pan, Y. Su, X. Song, J. Cao, H. Chen, W. Li, *J. Mater. Sci. Technol.*, 2026, 244, 46–59.
17. A. Bano, P. Li, Z. Qin, Z. Zhang, W. Han, X. Jiang, H. Dong, *Sci. Technol. Weld. Join.*, 2025, 30, 46–54.
18. X. Jiang, H. Dong, L. Zhang, Z. Qin, Y. Wang, B. Zhao, P. Li, *Mater. Charact.*, 2025, 220, 114662.
19. J. Chen, J. Dong, Y. Wei, Y. Guo, X. Wang, *Weld. World.*, 2024, 68, 23–34.
20. Y. Zhang, Y. Zhong, Y. Cheng, N. He, L. He, Z. Gao, X. Gong, C. Chen, H. Ye, *J. Mater. Sci. Technol.*, 2024, 185, 9–22.
21. Y. Zhang, Y. Cheng, Y. Zhong, N. He, L. He, Z. Gao, X. Gong, C. Chen, H. Ye, *Mater. Sci. Eng. A.*, 2024, 892, 146071.
22. L. Zhang, C. Wang, Y. Zhang, Q. Guo, R. Ma, J. Zhang, S. Na, *Mater. Des.*, 2019, 182, 108002.
23. Z. W. Yang, J. Lian, J. Wang, X. Q. Cai, Y. Wang, D. P. Wang, Z. M. Wang, Y. C. Liu, *J. Alloys Compd.*, 2020, 819, 153324.
24. C. A. Tadgell, S. F. Corbin, *J. Mater. Sci.*, 2021, 56, 10597–10613.
25. B. Wu, H. Dong, Y. Ma, P. Li, C. Li, L. Huang, L. Zhang, J. Li, *Mater. Sci. Eng. A.*, 2023, 887, 145737.
26. M. Tashiro, S. Sukenaga, K. Ikemoto, K. Shinoda, T. Kajitani, S. Suzuki, H. Shibata, *J. Mater. Sci.*, 2021, 56, 16545–16557.
27. J. Song, S. Xu, Z. Lu, Y. Peng, Y. Du, J. Xiong, J. Li, *Mater. Today Commun.*, 2025, 47, 113275.
28. Q. Yin, Z. Yang, H. Li, H. Du, *J. Magnes. Alloy.*, 2025, 13, 3166–3185.
29. W. Guo, J. Xin, D. Hao, Y. Ma, J. Xiong, J. Li, Q. Feng, *J. Mater. Res. Technol.*, 2026, 30, 267-282.
30. X. Hong, Z. Qin, X. Jiang, J. Wang, J. Li, Z. Ding, J. Wang, S. Shi, P. Li, H. Dong, *Mater. Horiz.*, 2026. https://doi.org/10.1039/D5MH01841B
31. I. Povstugar, P. Choi, S. Neumeier, A. Bauer, C. H. Zenk, M. Göken, D. Raabe, *Acta Mater.*, 2014, 78, 78–85.
32. J. Zhang, Q. Na, T. Ma, F. Lu, R. Li, J. Wang, C. Wang, G. Zhang, H. Su, L. Liu, *Mater. Sci. Eng. A.*, 2025, 932, 148250.
33. Y. Wang, Z. Ding, P. Li, Z. Qin, X. Bi, L. Zhang, C. Li, H. Dong, H. Sun, Y. Cheng, Y. S. Sato, *Compos. Part B Eng.*, 2025, 297, 112330.
34. W. J. Liu, H. Li, Q. X. Yin, H. J. Du, *Rare Met.*, 2024, 43, 4548–4565.
35. X. Hong, X. Jiang, Z. Qin, J. Wang, F. Jin, P. Li, H. Dong, *Sci. Technol. Weld. Join.*, 2025. https://doi.org/10.1177/13621718251394862
36. G. Wang, Y. Zhang, J. Liu, W. Chen, K. Wang, B. Cui, B. Zou, Q. Ouyang, Y. Zhang, Z. Hu, L. Wang, W. Yan, S. Jin, J. Ding, Y. Wang, T. Zhu, Z. Li, D. Zhang, E. Ma, *Nat. Commun.*, 2025, 16, 3589.
37. M. X. Zhang, P. M. Kelly, *Acta Mater.*, 2005, 53, 1073–1084.
38. W. Liu, J. Meng, J. Xiao, H. Li, L. Wu, Q. Yin, C. Tan, *Virtual Phys. Prototyp.*, 2024, 19, 1–22.
39. H. Wang, T. Harrington, C. Zhu, K. S. Vecchio, *Acta Mater.*, 2019, 175, 445–456.
40. J. Lin, Y. Chen, D. Ma, L. Xing, P. He, W. Yang, T. Lin, *J. Mater. Sci. Technol.*, 2026, 243, 192–205.
41. Z. Ding, P. Li, Z. Qin, W. Huang, P. Zhao, D. Zhou, X. Meng, Y. S. Sato, H. Dong, *Nano Lett.*, 2024, 24, 12171–12178.
42. J. Wang, Y. Wang, Z. Qin, P. Li, Z. Ding, Y. Sun, T. Li, *J. Manuf. Process.*, 2025, 149, 1126–1137.
43. Z. Qin, B. Zhao, Y. Wang, Z. Zhao, S. Liu, Z. Ding, L. Zhang, J. Wang, P. Li, H. Dong, *Mater. Lett.*, 2025, 401, 139175.
44. T. Lin, C. Li, D. Gao, Z. Du, X. Si, J. Qi, J. Cao, *J. Mater. Sci. Technol.*, 2024, 192, 228–239.
45. H. Yang, C. Li, X. Si, J. Qi, J. Cao, *Mater. Charact.*, 2024, 211, 113867.
46. Z. Qin, X. Ma, J. Li, Y. Zhao, Z. Zhang, C. Shan, H. Liu, Y. Qi, Y. Xie, X. Meng, Y. Huang, *J. Manuf. Process.*, 2024, 124, 1459–1470.
47. L. Zhou, S. Liu, J. Min, Z. W. Qin, W. X. He, X. G. Song, H. B. Xu, J. C. Feng, *Int. J. Miner. Metall. Mater.*, 2021, 28, 1506–1514.
48. H. Wu, W. Yang, H. Peng, X. Li, J. Chen, *J. Manuf. Process.*, 2020, 57, 477–487.
49. L. Yuan, J. Xiong, Y. Peng, Z. Li, J. Li, *Vacuum*, 2020, 173, 109120.
50. W. Li, Y. Liang, Y. Bai, T. Lin, B. Li, J. Feng, *J. Mater. Sci. Technol.*, 2023, 139, 210–223.
51. Y. Wang, Y. -T. Huang, Y. X. Liu, S. Feng, M. X. Huang, *Scr. Mater.*, 2022, 220, 114900